Nano Research 2018, 11(9): 4890–4904
https://doi.org/10.1007/s12274-018-2078-9
Research Article
ISSN 1998-0124
CN 11-5974/O4

General synthesis of silica-based yolk/shell hybrid nanomaterials and *in vivo* tumor vasculature targeting

Feng Chen[1], Shreya Goel[2], Sixiang Shi[2], Todd E. Barnhart[3], Xiaoli Lan[4] (✉), and Weibo Cai[1,2,3,5] (✉)

[1] *Department of Radiology, University of Wisconsin-Madison, WI 53705, USA*
[2] *Materials Science Program, University of Wisconsin-Madison, WI 53705, USA*
[3] *Department of Medical Physics, University of Wisconsin-Madison, WI 53705, USA*
[4] *Department of Nuclear Medicine, Union Hospital, Tongji Medical College, Huazhong University of Science and Technology, Wuhan 430022, China*
[5] *University of Wisconsin Carbone Cancer Center, Madison, WI 53705, USA*

Received: 23 February 2018
Revised: 14 April 2018
Accepted: 17 April 2018

KEYWORDS
yolk/shell,
intrinsic radiolabeling,
vasculature targeting,
positron emission tomography,
zirconium-89

ABSTRACT

Multifunctional yolk/shell-structured hybrid nanomaterials have attracted increasing interest as theranostic nanoplatforms for cancer imaging and therapy. However, because of the lack of suitable surface engineering and tumor targeting strategies, previous research has focused mainly on nanostructure design and synthesis with few successful examples showing active tumor targeting after systemic administration. In this study, we report the general synthetic strategy of chelator-free zirconium-89 (^{89}Zr)-radiolabeled, TRC105 antibody-conjugated, silica-based yolk/shell hybrid nanoparticles for *in vivo* tumor vasculature targeting. Three types of inorganic nanoparticles with varying morphologies and sizes were selected as the internal cores, which were encapsulated into single hollow mesoporous silica nanoshells to form the yolk/shell-structured hybrid nanoparticles. As a proof-of-concept, we demonstrated successful surface functionalization of the nanoparticles with polyethylene glycol, TRC105 antibody (specific for CD105/endoglin), and ^{89}Zr (a positron-emitting radioisotope), and enhanced *in vivo* tumor vasculature-targeted positron emission tomography imaging in 4T1 murine breast tumor-bearing mice. This strategy could be applied to the synthesis of other types of yolk/shell theranostic nanoparticles for tumor-targeted imaging and drug delivery.

1 Introduction

Despite great challenges in the clinical translation of nanomedicine [1–3], scientists worldwide are devoting great efforts in searching for various types of multifunctional nanomaterials to improve future cancer management. The last decade has witnessed an unprecedented expansion in the design, synthesis, and preclinical applications of various kinds of nanomaterials [4, 5]. Among them, silica-based hybrid nanoparticles have shown immense potential in targeted

Address correspondence to Xiaoli Lan, LXL730724@hotmail.com; Weibo Cai, wcai@uwhealth.org

cancer diagnosis and therapy [6, 7]. Silica, or silicon dioxide, is "generally recognized as safe" by the U.S. Food and Drug Administration (ID Code: 14808-60-7) [8]. To date, the silica-shell-coating strategy remains one of the most used, economical, and practical techniques for the design and synthesis of hybrid nanomaterials [9]. Ultra-small dye-encapsulated fluorescent silica nanoparticles, known as C dots (or "Cornell dots"), entered clinical trials in January 2011 (NCT01266096, NCT02106598) [10, 11]. These "target-or-clear" hybrid silica nanostructures (< 10 nm) are encapsulated with near-infrared (NIR) dyes (e.g. Cy5), tumor-homing peptides (e.g. cRGDY), and radioisotopes (e.g. iodine-124 (^{124}I, $t_{1/2}$ = 100.8 h) and zirconium-89 (^{89}Zr, $t_{1/2}$ = 78.4 h)), allowing for positron emission tomography (PET)-/optical dual-modality-targeted imaging of cancer [10, 12–14]. Besides its high clinical translational potential, silica is also known as a versatile nanoplatform for intrinsic radiolabeling [15, 16]. Recently, we and others have successfully developed a silica-based intrinsic radiolabeling technique for isotopes of ^{89}Zr [15, 16], copper-64 (^{64}Cu, $t_{1/2}$ = 12.7 h) [17], arsenic-72 (^{72}As, $t_{1/2}$ = 26 h) [18], and titanium-45 (^{45}Ti, $t_{1/2}$ = 3.1 h) [19], to name a few.

Biocompatible porous silica nanoparticles, such as mesoporous silica nanoparticles (MSNs), with a relatively larger particle size (> 50 nm) than that of C dots (< 10 nm) have been attractive drug delivery systems because of their high specific surface area and pore volume [20–24]. By introducing a large cavity inside each original MSN, hollow mesoporous silica nanoparticles (HMSNs) have attracted increasing interest as a new drug delivery system with greatly enhanced drug loading capacity [25, 26]. To further integrate other optical or magnetic functionalities, a new type of hybrid nanomaterial, named yolk/shell-structured nanoparticles, has also been developed [27–33]. Each hybrid nanoparticle possesses an inorganic functional core for imaging or therapy, a large cavity for the storage of chemotherapeutic drugs, and a thin mesoporous silica shell with tunable pore size for facilitating the loading and release of the pre-loaded drugs [34].

Efficient targeting of these silica-based hybrid nanomaterials to the tumor site is critical. The focus of previous research on yolk/shell-structured nanoparticles was mainly on the nanoparticle design and synthesis [8, 35, 36]. However, because of the lack of suitable surface engineering and tumor targeting strategies, very few of them showed the capability of *in vivo* whole-body biodistribution and active tumor-targeted imaging. Tumor vessels are known to have high vascular permeability and lack functional lymphatics because of the uncontrolled growth rate and changes in endothelial cell shape, resulting in the accumulation of various nanoparticles (typically smaller than 300 nm) in tumor tissues based on the enhanced permeability and retention (EPR) effect [37]. Tumor vasculature targeting (i.e. targeting receptors overexpressed on tumor vascular endothelial cells) is a generally applicable targeting strategy for a wide variety of nanoparticles regardless of tumor type [38]. By targeting CD105 (also known as endoglin, which is an ideal marker that is almost exclusively overexpressed on proliferating endothelial cells [39]), we have demonstrated the broad potential of CD105-targeted nanomaterials in cancer-targeted imaging and therapy using TRC105, a human/murine chimeric IgG1 monoclonal antibody that binds to both human and murine CD105 [40], or its fragments as the targeting moieties [23, 25, 41–43].

In this work, we report the general synthesis strategy of chelator-free ^{89}Zr-radiolabeled, TRC105-conjugated, silica-based yolk/shell hybrid nanoparticle for *in vivo* tumor vasculature targeting. Three types of inorganic nanoparticles with varying morphologies and sizes were selected as the internal cores, which were encapsulated into single HMSNs to form the yolk/shell-structured hybrid nanoparticles. As a proof-of-concept, we showed the successful post-surface functionalization of the nanoparticles with polyethylene glycol (PEG), TRC105, and ^{89}Zr, and demonstrated the *in vivo* tumor vasculature-targeted PET imaging in 4T1 murine breast tumor-bearing mice. This strategy could be applicable to the synthesis of other types of yolk/shell nanoparticles, creating an attractive multifunctional nanoplatform for tumor-targeted imaging and drug delivery.

2 Results and discussion

2.1 General synthesis of multi-functional yolk/shell-structured hybrid nanomaterials

As shown in Scheme 1, the general synthesis of yolk/

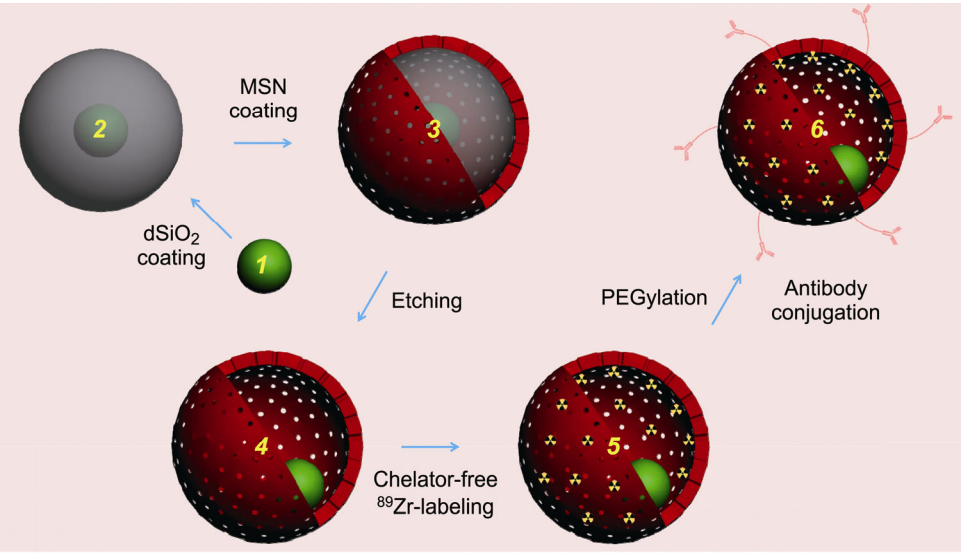

Scheme 1 General synthesis of multi-functional yolk/shell-structured hybrid nanomaterials. Pre-prepared inorganic functional nanocrystal (**1**, such as UCNP, SPION, or QD) was selected as the core and coated with dense silica to form core@$dSiO_2$ (**2**). The nanoparticle was further coated with another layer of mesoporous silica nanoshell, forming core@$dSiO_2$@MSN (**3**). A selective etching strategy was then introduced to selectively etch the $dSiO_2$ layer while leaving the MSN layer intact, forming core@HMSN (**4**, where HMSN stands for hollow mesoporous silica nanoshell). Because of the presence of abundant silanol groups (–Si–OH) on the surface and inside the meso-channels of core@HMSN, ^{89}Zr could be labeled to the nanoparticles without using any extra chelators, forming core@[^{89}Zr]HMSN (**5**). The nanoparticle was finally modified with PEG and tumor vasculature-targeted antibody (e.g. TRC105) to form core@[^{89}Zr]HMSN-PEG-TRC105 (**6**).

shell-structured tumor vasculature-targeted silica-based hybrid nanoparticles started with a surfactant-stabilized (e.g. oleic acid) inorganic functional nanoparticle (e.g. upconversion nanoparticle (UCNP), superparamagnetic iron oxide nanoparticle (SPION), or quantum dot (QD)) as the internal core. Subsequently, an oil-in-water reverse micro-emulsion silica coating approach was introduced to uniformly coat each hydrophobic nanoparticle core with a thickness-controllable and biocompatible non-porous silica interlayer. This step will facilitate the coating of the third porous silica outer layer with the presence of template surfactants (e.g. cetyltrimethylammonium chloride solution, or CTAC). A selective silica etching protocol was then adopted to carefully etch out the non-porous silica interlayer, leaving a cavity inside each ~ 100-nm yolk/shell nanoparticle. Afterwards, a silica-based chelator-free ^{89}Zr labeling strategy was employed to stably radiolabel the nanoparticle with ^{89}Zr for *in vivo* whole-body PET imaging. The radiolabeled nanoparticles were then surface-PEGylated and functionalized with TRC105 to improve stability in the bloodstream and specific targeting of CD105 in the tumor vasculature.

2.2 Synthesis of UCNP@HMSN hybrid nanoparticles

UCNPs have gained growing interest owing to their unique upconversion luminescence features that are highly suitable for multimodal imaging in living subjects [44]. After excitation using a 980-nm laser, UCNPs exhibited attractive optical features, such as sharp emission lines [45], long lifetimes (~ ms) [46], large anti-Stokes shift [45], superior photo-stability [47], high detection sensitivity [48], non-blinking and non-bleaching [47, 49], deeper tissue penetration depth [50], minimal photo-damage [51], and extremely low auto-fluorescence [52]. In this study, we synthesized uniform ~ 25-nm UCNPs of β-$NaYF_4$:Tm/Yb (2/20 mol%) (Fig. 1(a)) using a modified procedure that has been reported previously [53, 54]. The inset in Fig. 1(a) shows a digital photo of β-$NaYF_4$:Tm/Yb (suspended in cyclohexane) emitting ultraviolet (UV), blue, and NIR light after excitation with a 980-nm laser (only the blue light was captured by a digital single-lens reflex (DSLR) camera). As-synthesized UCNPs were then coated with a dense silica ($dSiO_2$) shell in an oil-in-water reverse micro-emulsion system [55]. Figure 2(a) shows

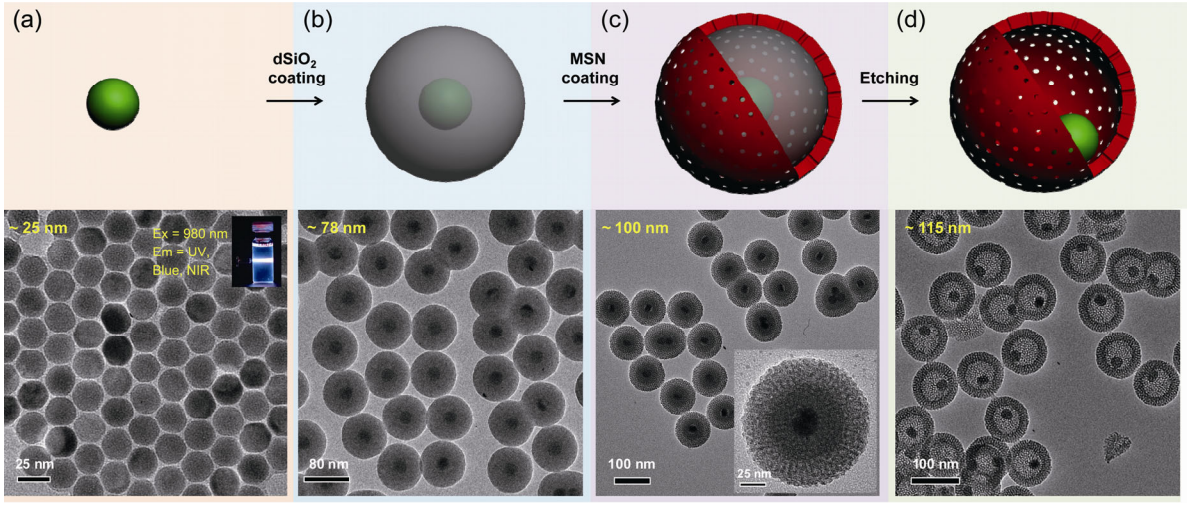

Figure 1 Synthesis of UCNP@HMSN hybrid nanoparticles. (a) Schematic illustration and TEM image of ~ 25-nm Tm/Yb co-doped UCNP ($NaYF_4$:Tm/Yb). Inset is a digital photo showing the blue light emission of $NaYF_4$:Tm/Yb under the excitation of a 980-nm laser (captured by a DSLR camera). (b) Schematic illustration and TEM image of ~ 78-nm UCNP@$dSiO_2$. The thickness of the $dSiO_2$ layer was estimated to be ~ 14 nm. (c) Schematic illustration and TEM image of ~ 100-nm UCNP@$dSiO_2$@MSN. Inset is a single nanoparticle clearly showing the core (the inner dark dot), the first $dSiO_2$ layer (middle layer with a lighter color), and the second MSN layer (the outermost layer with the lightest color). The thickness of the MSN layer was estimated to be ~ 11 nm. (d) Schematic illustration and TEM image of ~ 115-nm UCNP@HMSN.

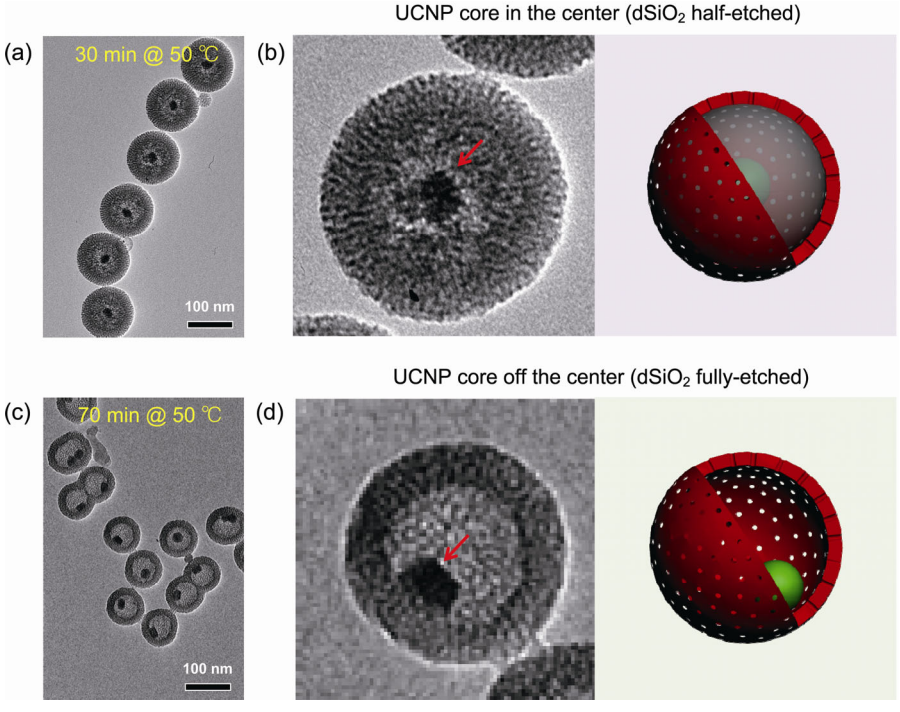

Figure 2 Optimization of the etching protocol. (a) TEM image of UCNP@HMSN synthesized by etching at 50 ℃ for 30 min. (b) TEM image of a single UCNP@HMSN with half-etched $dSiO_2$ (left) and its corresponding scheme (right). (c) TEM image of UCNP@HMSN synthesized by etching at 50 ℃ for 70 min. (d) TEM image of a single UCNP@HMSN with fully etched $dSiO_2$ (left) and its corresponding scheme (right). The UCNP cores are indicated by red arrows in both (b) and (d).

the transmission electron microscopy (TEM) image of ~ 78-nm UCNP@$dSiO_2$. The thickness of the $dSiO_2$ layer was estimated to be ~ 14 nm. The delivery rate of tetraethyl orthosilicate (TEOS) during the synthesis

of UCNP@$dSiO_2$ was found to have significant impact on the yield of UCNP@$dSiO_2$, which was carefully controlled at 100 μL·h^{-1} using a syringe pump to avoid aggregation and homogeneous nucleation of silica [55].

The introduction of the $dSiO_2$ layer is critical for the successful formation of the yolk/shell nanostructure. It not only facilities the growth of the third porous silica layer, but also serves as a hard template that will later be selectively etched out to form the cavity. To grow the third porous silica layer, as-synthesized UCNP@$dSiO_2$ suspended in deionized water were mixed with CTAC, triethanolamine (TEA), and TEOS. A slow and controllable TEOS delivery procedure (rate: 40 μL·min^{-1}) was again used in this case with a syringe pump. Figure 1(c) shows the TEM image of ~ 100-nm UCNP@$dSiO_2$@MSN. The inset is a single UCNP@$dSiO_2$@MSN showing the UCNP core (the inner dark dot), the first $dSiO_2$ layer (middle layer with a lighter color), and the second MSN layer (the outermost layer with the lightest color). The thickness of the third porous silica layer was found to be ~ 11 nm.

Before performing any nanoparticle purification procedures, the reaction system was cooled down to 50 °C, followed by the addition of sodium carbonate (Na_2CO_3), and kept under constant stirring for 30–70 min to selectively etch out the $dSiO_2$ interlayer, forming yolk/shell-structured UCNP@HMSN, as shown in Fig. 1(d). The final average size of UCNP@HMSN was measured to be ~ 115 nm. The surfactant CTAC was later removed via an extraction process by stirring the nanoparticles in a 1 wt.% solution of NaCl in methanol [56]. The pore size of the nanoparticle porous silica layer was 2–3 nm, similar to that of previously reported MSNs [23].

2.3 Optimization of the selective silica etching procedure

Cationic surfactants (in our case, CTAC) play vital roles in the formation of the yolk/shell nanostructure. It is important to note that CTAC needs to stay in the MSN network to ensure successful selective etching of $dSiO_2$. During the etching process, positively charged free cetyltrimethylammonium cations (CTA^+) will first adsorb to the surface of UCNP@$dSiO_2$@MSN(CTAC) via electronic attraction. Subsequently, with the presence of Na_2CO_3 in the solution and CTAC in the MSN shell, selective etching of silica from the $dSiO_2$ core starts and will be accelerated by the surrounding free CTAC, forming uniform UCNP@HMSN(CTAC) after the re-deposition process [57]. The effective etching of the $dSiO_2$ interlayer was demonstrated to be highly dependent on the free CTAC concentration, etching temperature, and etching time, as we reported previously [25]. To avoid over-etching, the optimal etching temperature was fixed to be 50 °C. Figures 2(a) and 2(b) show the representative TEM images of UCNP@HMSN with nearly half of the $dSiO_2$ being etched out. The UCNP core was still in the center of the nanoparticle, supported by the $dSiO_2$ network. Prolonging the etching time to 70 min while keeping the same etching temperature could lead to complete etching of the $dSiO_2$ interlayer, causing the inner UCNP to move to the wall of the MSN layer because of the lack of $dSiO_2$ support, as shown in Figs. 2(c) and 2(d).

2.4 Synthesis of other types of yolk/shell hybrid nanomaterials with irregularly shaped cores

To demonstrate the general applicability of the above-mentioned strategy, we extended the uniform 25-nm UCNP cores to other nanoparticles with irregular shapes and smaller sizes. Oleic acid-capped SPIONs with an average particle size of 8–10 nm were synthesized based on a previously reported thermal decomposition approach [55, 58]. As shown in Fig. 3(a), as-synthesized SPIONs had a relatively broad size distribution and non-spherical morphology. The inset in Fig. 3(a) shows the clear superparamagnetism of SPIONs suspended in cyclohexane at room temperature. The third functional nanocrystal core we selected was the commercially available organic QD705 (1 μM in decane, purchased from Life Technology). A representative TEM image of QD705 (Fig. 3(d)) revealed a rod-shaped QD705 with dimensions of ~ 6.5 nm × ~ 13 nm. The inset in Fig. 3(d) is a photo showing the optical imaging (Em = 700 nm) of QD705 under blue light excitation (Ex = 465 nm) using an IVIS Spectrum imaging system. Successful formation of monodispersed yolk/shell-structured SPION@HMSN and QD705@HMSN was found to be highly dependent on the $dSiO_2$ coating step (Figs. 3(b) and 3(e)), where severe nanoparticle aggregation should be avoided to improve the yield

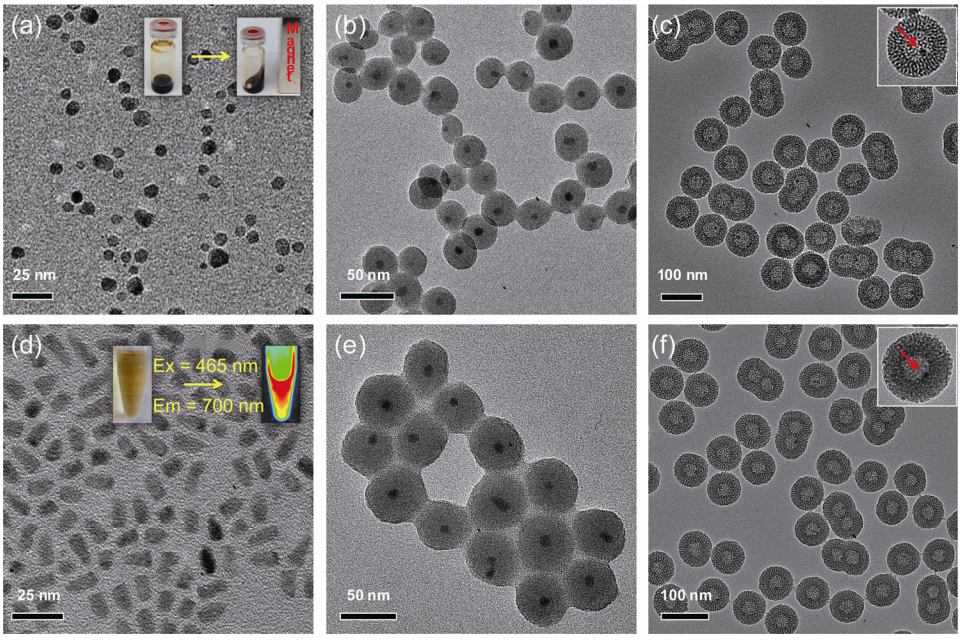

Figure 3 Synthesis of SPION@HMSN and QD@HMSN. (a) TEM image of oleic acid-capped SPIONs. Inset is a photo showing the ferrofluidic behavior of SPIONs in cyclohexane at room temperature. (b) TEM image of SPION@dSiO$_2$. (c) TEM image of SPION@HMSN. Inset shows a single SPION@HMSN, where the SPION core is indicated by a red arrow. (d) TEM image of organic QD705 purchased from Life Technology. Inset is a photo showing the optical imaging of QD705 using an IVIS Spectrum system (Ex = 465 nm, Em = 700 nm). (e) TEM image of QD705@dSiO$_2$. (f) TEM image of QD705@HMSN. Inset shows a single QD705@HMSN, where the QD705 core is indicated by a red arrow.

and stability of the final hybrid nanoparticles (Fig. S1 in the Electronic Supplementary Material (ESM)). The final sizes of SPION@HMSN and QD705@HMSN measured by TEM were ~ 77 and ~ 67 nm, respectively, which were significantly smaller than the ~ 115-nm UCNP@HMSN. Because of the smaller core size and greater difficulties in achieving monodispersed core@dSiO$_2$ nanoparticles, higher yields of twins and triplets (Figs. 3(c) and 3(f)) were observed in these two cases when compared with UCNP@HMSN (as shown in Fig. 1(d)). Taken together, we demonstrated the successful extension of the yolk/shell hybrid nanoparticle synthesis to other functional (magnetic and optical) nanoparticles with varying sizes and morphologies.

2.5 Surface functionalization of UCNP@HMSN for *in vitro* CD105 targeting

To demonstrate the active targeting of a representative yolk/shell hybrid nanomaterial, as-synthesized uniform UCNP@HMSN were selected and subjected to post-surface functionalization, which included amination, PEGylation, and antibody conjugation based on previously reported procedures [23, 25, 43]. Without suitable PEGylation, the highly negatively charged UCNP@HMSN could form severe aggregation in phosphate-buffered saline (PBS) within minutes. The stability was significantly improved after surface PEGylation. The hydrodynamic diameter (HD) of the final UCNP@HMSN-PEG$_{5k}$-TRC105 was measured to be 171.9 ± 1.2 nm by dynamic light scattering (DLS), as shown in Fig. 4(a).

Before *in vivo* investigation, human umbilical vein endothelial cells (HUVECs, CD105-positive) were subjected to flow cytometry to confirm the *in vitro* CD105 targeting efficiency of the non-radioactive UCNP@HMSN-PEG$_{5k}$-TRC105. Because of the lack of a 980-nm excitation light source in the BD FACSCalibur four-color analysis cytometer, which was equipped with 488-nm and 633-nm lasers, NHS-fluorescein was conjugated to the surface of the nanoparticles to facilitate the flow cytometry study. The results from Fig. 4(b) indicated that incubation with fluorescein-conjugated UCNP@HMSN-PEG$_{5k}$-TRC105 (50 nM, targeted group) could significantly enhance the mean fluorescence intensity of HUVECs, while treatment with fluorescein-conjugated UCNP@HMSN-PEG$_{5k}$ (50 nM, non-targeted group) or fluorescein-conjugated UCNP@HMSN-PEG$_{5k}$-TRC105 with a blocking

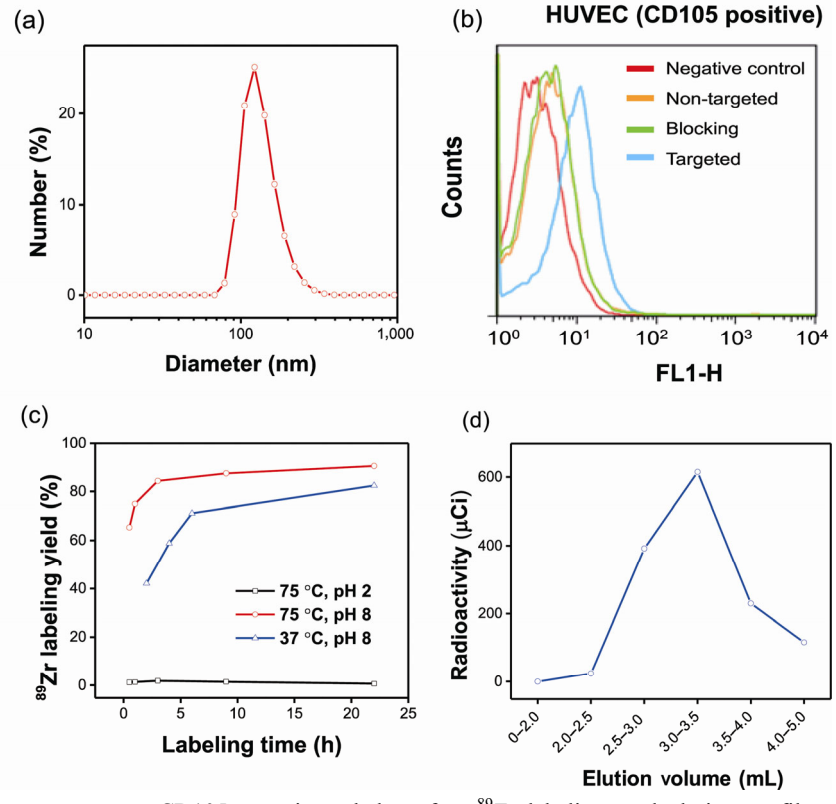

Figure 4 DLS measurement, *in vitro* CD105 targeting, chelator-free ^{89}Zr labeling, and elution profile of UCNP@[^{89}Zr]HMSN-PEG$_{5k}$-TRC105. (a) Size distribution of UCNP@HMSN-PEG$_{5k}$-TRC105 measured by DLS. (b) Flow cytometry analysis of fluorescein-conjugated UCNP@HMSN-PEG$_{5k}$-TRC105 (50 nM, 30 min incubation) in HUVECs (CD105-positive). (c) ^{89}Zr labeling yields of UCNP@HMSN at varying temperatures in solutions of different pH values. (d) A PD-10 elution profile of UCNP@[^{89}Zr]HMSN-PEG$_{5k}$-TRC105. PBS was used as the mobile phase.

dose of TRC105 (500 μg·mL^{-1}, blocking group) only yielded minimal fluorescence enhancement via non-specific binding.

2.6 Chelator-free ^{89}Zr labeling and *in vivo* CD105-targeted PET imaging

Zr^{4+} is a hard Lewis acid and thus prefers hard Lewis bases as donor groups. Previously, we demonstrated that the deprotonated silanol groups (–Si–O$^-$), which originated from the hydrolysis and condensation of TEOS [59], could function as hard Lewis bases for stable chelator-free ^{89}Zr labeling of silica-based nanoparticles [15]. Approximately 2–3 million –Si–OH groups in each 150-nm MSN was estimated based on our previous research [15]. For typical chelator-free radiolabeling, aminated UCNP@HMSN (or UCNP@HMSN-NH_2, concentration: ~ 1 mg·mL^{-1}) were suspended in 4-(2-hydroxyethyl)-1-piperazineethanesulfonic acid (HEPES) buffer (pH 7.5, 0.1 M) and mixed with 3 mCi (or 111 MBq) of ^{89}Zr-oxalate at 75 °C for 3 h. The final pH of the mixture was carefully re-adjusted to 7–8 with 2 M Na_2CO_3. The labeling yield was found to be greater than 80% after labeling at 75 °C for 3 h. The yield continued to increase over time and reached > 90% after 22 h of incubation (Fig. 4(c) and Table S1 in the ESM). Such ^{89}Zr labeling was also found to be concentration- and temperature-dependent, with higher concentration and incubation temperature giving higher labeling yield, similar to what we have observed previously [15]. For example, slightly reduced labeling yield over time was achieved by lowering the labeling temperature to 37 °C, as shown in Table S2 in the ESM. To further demonstrate the role of deprotonated silanol groups in chelator-free ^{89}Zr labeling, the pH of the labeling solution was adjusted to near the isoelectric point of silica, which is approximately 2, to ensure protonation of the silanol groups as –Si–OH. As expected, the ^{89}Zr labeling yield was almost completely inhibited,

with the maximal labeling yield found to be lower than 2%, as shown in Table S1 in the ESM. As-synthesized UCNP@[^{89}Zr]HMSN-NH_2 was easily collected by centrifugation and readily PEGylated by reacting with SCM-PEG_{5k}-Mal (SCM denotes succinimidyl carboxy methyl ester; Mal denotes maleimide) (5 mg) at pH 7 for 2 h, forming UCNP@ [^{89}Zr]HMSN-PEG_{5k}-Mal. UCNP@[^{89}Zr]HMSN-PEG_{5k}-TRC105 was finally obtained by reacting UCNP@ [^{89}Zr]HMSN-PEG_{5k}-Mal with TRC105-SH in PBS at room temperature, as reported previously [23, 41]. Figure 4(d) shows the representative PD-10 elution profile of UCNP@[^{89}Zr]HMSN-PEG_{5k}-TRC105 (PBS was used as the mobile phase), with the products eluted from 2.5 mL to 4.0 fractions. These fractions were collected for further *in vivo* tumor-targeted PET imaging and *ex vivo* biodistribution experiments.

In vivo tumor-targeted PET imaging was then carried out in 4T1 murine breast tumor-bearing mice, which express high levels of CD105 in the tumor neovasculature [60]. Each mouse was injected with 5–10 MBq of ^{89}Zr-labeled yolk/shell nanoparticles, and time points of 0.5, 6, 24, and 48 h post-injection (p.i.) were chosen for serial PET scans to show the *in vivo* biodistribution patterns of tumor-bearing mice from targeted, non-targeted, and blocking groups (Fig. 5). Quantitative data obtained from region-of-interest (ROI) analysis of these PET images are also shown in Fig. 5 and Tables S3–S5 in the ESM. The circulation of the ^{89}Zr-labeled nanoparticles in all three groups was indicated by the dominant radioactivity signal in mouse heart (or blood) at 0.5 h p.i., with the radioactivity signal in the heart ranging from 22.6 %ID·g^{-1} (percentage of the injected dose per gram) to 30.5 %ID·g^{-1} (Tables S3–S5 in the ESM). The clearance of the nanoparticles from blood to the liver and spleen was also observed among these groups, with a clear decrease in radioactive signal in the bloodstream and rapid accumulation of nanoparticles in the mouse reticuloendothelial system (RES) (Fig. 5). The blood circulation half-life of UCNP@[^{89}Zr]HMSN-PEG_{5k}-TRC105 in 4T1 tumor-bearing mice was estimated to be approximately 4.5 h based on the PET data.

The accumulation of UCNP@[^{89}Zr]HMSN-PEG_{5k}-TRC105 in the 4T1 tumor was found to be 2.4 ± 0.3 %ID·g^{-1} at 0.5 h p.i., and peaked at 10.0 ± 0.9 %ID·g^{-1} at 6 h p.i., as shown in Figs. 5(a) and 6(a), and Table S3 in the ESM (n = 3). In contrast, without the conjugation of TRC105 (i.e. passive targeting alone), the 4T1 tumor uptake of

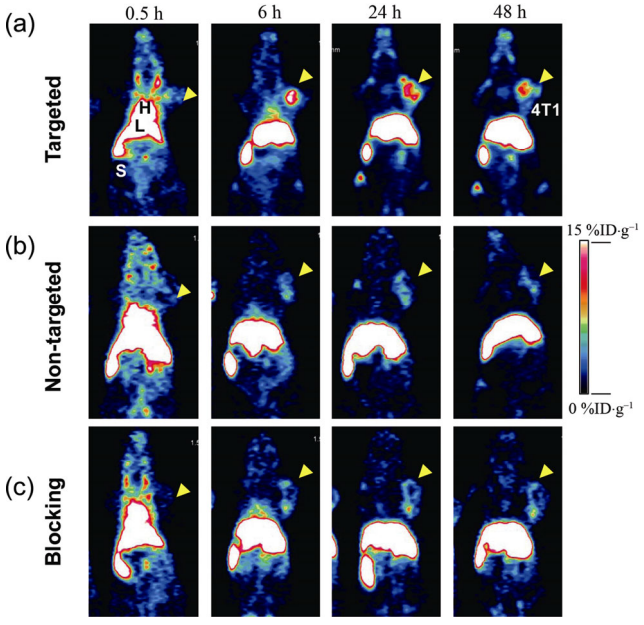

Figure 5 *In vivo* CD105-targeted PET imaging. Serial coronal PET images of UCNP@[^{89}Zr]HMSN-PEG_{5k}-TRC105 ((a), targeted group), UCNP@[^{89}Zr]HMSN-PEG_{5k} ((b), non-targeted group), and UCNP@[^{89}Zr]HMSN-PEG_{5k}-TRC105 with 1 mg of free TRC105 ((c), blocking group) in 4T1 murine breast tumor-bearing mice at different time points (0.5, 6, 24, and 48 h p.i.) n = 3 for all these groups.

UCNP@[^{89}Zr]HMSN-PEG_{5k} was found to be only about half that of the targeted group at all time points examined (n = 3, Figs. 5(b) and 6(b), and Table S4 in the ESM), indicating that TRC105 conjugation could be the controlling factor for enhanced tumor accumulation of UCNP@[^{89}Zr]HMSN-PEG_{5k}-TRC105. To further confirm the CD105 targeting specificity for UCNP@[^{89}Zr]HMSN-PEG_{5k}-TRC105 *in vivo*, blocking studies were performed. Administration of a blocking dose (1 mg/mouse) of free TRC105 at 1 h before UCNP@[^{89}Zr]HMSN-PEG_{5k}-TRC105 injection significantly reduced the tumor uptake to 4.3 ± 0.7 %ID·g^{-1} at 6 h p.i. (n = 3, Figs. 5(c) and 6(c), and Table S5 in the ESM), clearly demonstrating the specificity of CD105 toward UCNP@[^{89}Zr]HMSN-PEG_{5k}-TRC105 *in vivo*. Figure 6(d) also summarizes the comparison of 4T1 tumor uptake in the three groups at different time points, where UCNP@[^{89}Zr]HMSN-PEG_{5k}-TRC105 shows the highest tumor uptake throughout the study period (**p < 0.005). Similar to what we have observed previously with TRC105-conjugated nanoparticles with similar HDs (50–200 nm) [23, 25, 41], besides tumor accumulation, most of the ^{89}Zr-labeled nanoparticles were taken up by the RES with liver

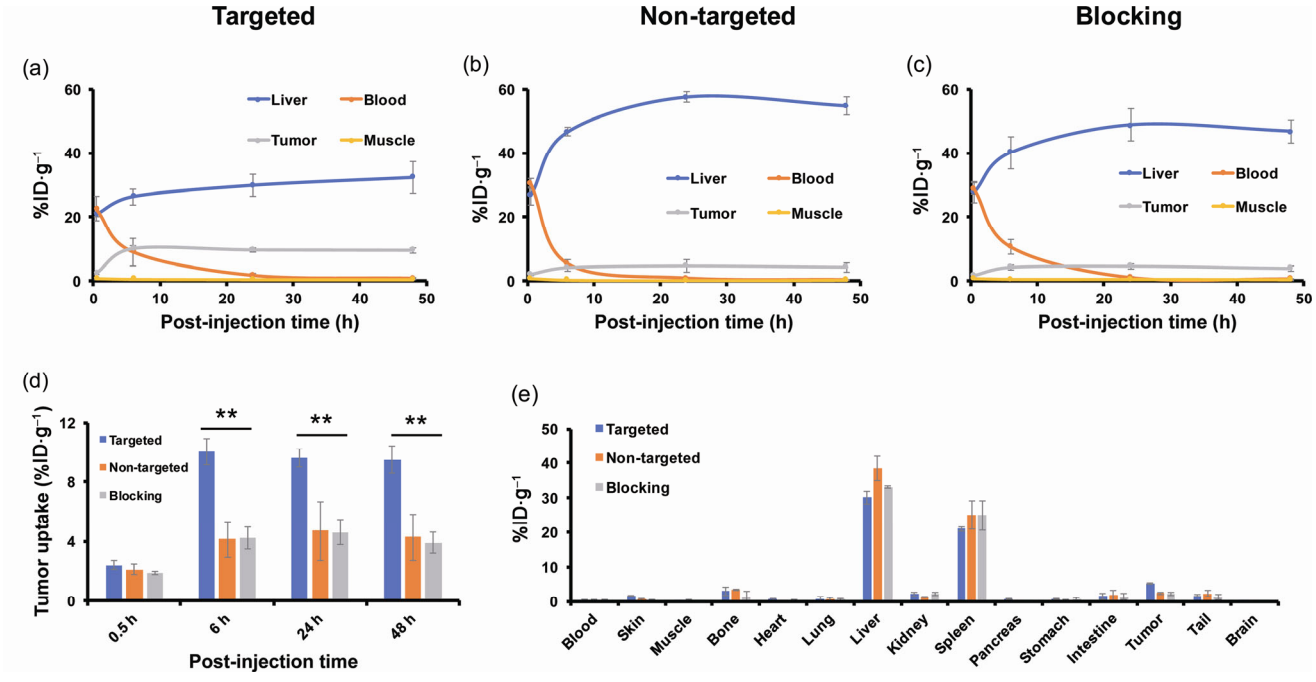

Figure 6 Quantitative ROI analysis of the PET imaging data and *ex vivo* biodistribution studies. Time–activity curves of the liver, blood, 4T1 tumor, and muscle upon intravenous injection of (a) UCNP@[^{89}Zr]HMSN-PEG$_{5k}$-TRC105, (b) UCNP@[^{89}Zr]HMSN-PEG$_{5k}$, or (c) UCNP@[^{89}Zr]HMSN-PEG$_{5k}$-TRC105 after a blocking dose (1 mg per mouse) of TRC105. (d) Comparison of 4T1 tumor uptake among the three groups. The difference in 4T1 uptake between UCNP@[^{89}Zr]HMSN-PEG$_{5k}$-TRC105 and the two control groups was statistically significant (**$p < 0.005$). (e) Biodistribution comparison in 4T1 tumor-bearing mice at 48 h p.i. All data represent three mice per group.

uptake found to be 20.7 ± 0.7 %ID·g^{-1} at 0.5 h p.i., and further increased to 32.3 ± 4.9 %ID·g^{-1} at 48 h p.i. for the targeted group (n = 3, Fig. 6(a) and Table S3 in the ESM). The maximal liver uptake was found to be even higher for the non-targeted (54.9 ± 2.7 %ID·g^{-1} at 48 h p.i., Fig. 6(b) and Table S4 in the ESM) and blocking group (46.9 ± 3.6 %ID·g^{-1} at 48 h p.i., Fig. 6(c) and Table S5 in the ESM). Figure 6(e) and Table S6 (in the ESM) summarize the biodistribution data of the ^{89}Zr-labeled nanoparticles at 48 h after the last PET scans. Overall, the quantitative results matched well with PET ROI analysis except that of 4T1 tumors due to the significantly enlarged tumor volume at 48 h p.i. High RES uptake and potential toxicity are two of the major issues for the different types of nanoparticles with HDs of > 10 nm during clinical translation. The current design of the UCNP@[^{89}Zr]HMSN-PEG$_{5k}$-TRC105 has a HD of ~ 200 nm and was expected to have high non-specific RES uptake, as shown in Figs. 5 and 6. Although no systematic and long-term toxicity studies were performed here, both the core (UCNPs, Fe_3O_4, and QDs) and the mesoporous silica shell were considered relatively safe, as demonstrated repeatedly in other research work [61–66].

3 Conclusion

In conclusion, to address the challenges in the synthesis, whole-body biodistribution, and *in vivo* active tumor targeting of silica-based hybrid nanoparticles, we report the general synthesis of three types of uniform yolk/shell-structured nanoparticles and present the chelator-free radiolabeling and *in vivo* tumor vasculature-targeted PET imaging of UCNP@[^{89}Zr]HMSN-PEG$_{5k}$-TRC105 in 4T1 tumor-bearing mice. Vascular targeting led to > 2-fold enhancement in tumor uptake compared to that of passive targeting alone based on the EPR effect (~ 10 %ID·g^{-1} vs. ~ 5 %ID·g^{-1}). Despite great challenges in the clinical translation of nanomedicine, we believe that the reported strategy might provide a highly valuable tool for scientists to create other attractive yolk/shell-structured multifunctional nanoplatforms for future tumor-targeted imaging and image-guided drug delivery.

4 Methods

4.1 Materials

TRC105 was provided by TRACON Pharmaceuticals Inc. (San Diego, CA). Chelex 100 resin (50–100 mesh), tetraethyl orthosilicate (TEOS), triethanolamine (TEA), (3-aminopropyl)triethoxysilane (APTES), cetyltrimethylammonium chloride solution (CTAC, 25 wt.%), absolute ethanol, sodium chloride (NaCl), sodium hydroxide (99.99%), oleic acid, 1-octadecene (technical grade, 90%), ammonia, yttrium(III) chloride hexahydrate, ytterbium(III) chloride hexahydrate, thulium(III) chloride, Igepal CO-520, and ammonium fluoride were obtained from Sigma-Aldrich and used without further purification. Iron chloride hexahydrate ($FeCl_3·6H_2O$, > 99%) was purchased from Acros. PD-10 columns were purchased from GE Healthcare (Piscataway, NJ). SCM-PEG_{5k}-Mal was obtained from Creative PEGworks. QD705 (1 μM in decane) was purchased from Life Technology. Water and all buffers were of Millipore grade and pretreated with Chelex 100 resin to ensure that the aqueous solution was free of heavy metals.

4.2 Synthesis of oleic acid-capped upconversion nanoparticles ($NaYF_4$:Tm/Yb)

Uniform-sized $NaYF_4$:Tm/Yb UCNPs were synthesized via a modified procedure that was reported previously [53, 54]. In a typical synthesis of 25-nm β-$NaYF_4$:Tm/Yb (2/20 mol%), $YCl_3·6H_2O$ (473.24 mg, 1.56 mmol), $YbCl_3·6H_2O$ (155 mg, 0.4 mmol), and $TmCl_3·6H_2O$ (11 mg, 0.04 mmol) in deionized water were added to a 100-mL flask containing 15 mL of oleic acid and 30 mL of 1-octadecene. The solution was then stirred at room temperature for 1 h. Afterwards, the mixture was slowly heated to 120 ℃ to remove water under an argon atmosphere. The solution was maintained at 156 ℃ for approximately 30 min until a homogeneous transparent yellow solution was obtained. The system was then cooled down to room temperature in argon. Subsequently, 10 mL of methanol solution of NH_4F (296.3 mg, 8 mmol) and NaOH (200 mg, 5 mmol) was added, and the solution was stirred at room temperature for another 2 h. After methanol was evaporated, the solution was heated to 290 ℃ and kept for 2 h before it was cooled down to room temperature. The resulting nanoparticles were precipitated by the addition of 20 mL of ethanol and collected by centrifugation at 10,000 rpm for 10 min. The product was re-dispersed with 5 mL of cyclohexane and precipitated again by adding 15 mL of ethanol, then collected by centrifugation at 10,000 rpm for 10 min. After four washes, the final product was well dispersed in 20 mL of cyclohexane.

4.3 Synthesis of oleic acid-capped SPIONs

A previously reported two-step synthetic approach [55, 58] was used in this work for the synthesis of SPIONs.

4.3.1 Step 1: synthesis of iron-oleate complex

Iron-oleate complex was used as the precursor for the synthesis of SPIONs. $FeCl_3·6H_2O$ (3.243 g, 12 mmol) and NaOH (1.44 g, 36 mmol) were dissolved in methanol (40 mL) under magnetic stirring. Oleic acid (12 mL, 36 mmol) was added to the $FeCl_3$-methanol solution, followed by addition of NaOH-methanol solution using a separatory funnel. The mixture was stirred overnight at room temperature. A reddish-brown product was found at the bottom of the mixture the next morning. The product was washed twice with methanol and twice with deionized water before it was dried at room temperature for 48 h. The final iron-oleate complex was obtained in a waxy solid form.

4.3.2 Step 2: synthesis of SPIONs

In a typical synthesis of 8–10 nm SPIONs, pre-prepared iron-oleate (2.9 g, ~ 3 mmol) was dissolved in 1-octadece (40 mL). The mixture was first heated to 80 ℃ to accelerate the dissolution of solid iron-oleate. It was then heated to 120 ℃ and maintained at this temperature for 2 h to remove air and water in the system. The reaction mixture was then directly heated to 300 ℃ and kept for 30 min. No extra oleic acid was used during the synthesis process. The black-brown mixture was cooled down to room temperature, washed with hexane and ethanol, and separated by magnetic separation. The final product was well dispersed in cyclohexane.

4.4 Synthesis of UCNP@HMSN

A three-step synthetic procedure was employed for the synthesis of UCNP@HMSN (or SPION@HMSN, QD@

HMSN).

4.4.1 Step 1: synthesis of UCNP@dSiO$_2$

To synthesize dense silica-coated UCNP (UCNP@dSiO$_2$) with a ~ 14-nm silica shell, Igepal CO-520 (NP-5, 2 mL) was dispersed in cyclohexane (40 mL) in a 100-mL three-necked flask and stirred for 5 min. Subsequently, oleic acid-capped UCNPs in cyclohexane solution (1 mL) was added into the cyclohexane/NP-5 mixture and stirred for 2 h at room temperature. Further, ammonia (280 μL, 30%) was added, and the system was sealed and stirred for another 2 h. TEOS (400 μL) was then delivered into the system at a rate of 100 μL·h^{-1} using a syringe pump. The mixture was sealed and kept under magnetic stirring for 48 h at room temperature before adding methanol to collect the nanoparticles. The product was precipitated with excess hexane and collected by centrifugation. The nanoparticles were re-dispersed in ethanol under ultrasonic treatment, precipitated with excess hexane, and collected by centrifugation. The process was repeated at least three times to completely remove the excess NP-5. The as-obtained UCNP@dSiO$_2$ were well-dispersed in ethanol or deionized water.

4.4.2 Step 2: synthesis of UCNP@dSiO$_2$@MSN

CTAC (2 g) and TEA (20 mg) were dissolved in 20 mL of high Q water and stirred at room temperature for 1 h. Subsequently, 10 mL of as-synthesized UCNP@dSiO$_2$ solution in water was added and stirred at room temperature for 1 h before the addition of 0.2 mL of TEOS using a syringe pump at 40 μL·min^{-1}. The mixture was stirred for 1 h at 80 °C in a water bath to form UCNP@dSiO$_2$@MSN.

4.4.3 Step 3: selective etching of the dSiO$_2$ interlayer to form UCNP@HMSN

The reaction system was cooled down to 50 °C followed by the addition of 636 mg of Na_2CO_3 and kept under constant stirring for 30–70 min to selectively etch out the dense silica layer, forming UCNP@HMSN. To remove the CTAC, the product was extracted for 24 h with a 1 wt.% solution of NaCl in methanol at room temperature. This process was carried out at least three times to ensure complete removal of CTAC. A similar three-step procedure was used for the synthesis of SPION@HMSN and QD@HMSN.

4.5 ^{89}Zr production

^{89}Zr-oxalate was produced according to previous procedures by the University of Wisconsin-Madison cyclotron group [67]. Briefly, natural yttrium-89 (^{89}Y) foil (250 μm, 99.9%) was irradiated with a proton beam to create ^{89}Zr via the ^{89}Y(p,n)^{89}Zr reaction using a 16-MeV GE PETtrace cyclotron (the actual proton beam energy used was ~ 13.8 MeV). After isotope separation and purification, ^{89}Zr-oxalate was obtained with a specific activity of > 20 GBq·μmol^{-1} of Zr.

4.6 Intrinsic ^{89}Zr labeling of UCNP@HMSN

The intrinsic radiolabeling of UCNP@HMSN with ^{89}Zr was based on the strong interaction between $^{89}Zr^{4+}$ and the abundant deprotonated silanol groups (–Si–O$^-$) from the HMSN shell [15]. For typical labeling, 250 μL of UCNP@HMSN at ~ 1 mg·mL^{-1} were suspended in HEPES buffer (pH 7.5, 0.1 M) and mixed with 3 mCi (or 111 MBq) of ^{89}Zr-oxalate at 75 °C for 3 h. The final pH of the mixture was carefully re-adjusted to 7–8 using 2 M Na_2CO_3. The labeling yield was found to be greater than 80% after labeling at 75 °C for 3 h. As-synthesized UCNP@[^{89}Zr]HMSN could be easily collected by centrifugation at 21,000*g* for 10 min. After washing three times with water, the final radioactive nanoparticles were well suspended in deionized water.

4.7 Synthesis of UCNP@[^{89}Zr]HMSN-PEG$_{5k}$-TRC105 for tumor vasculature targeting

To prepare UCNP@[^{89}Zr]HMSN-PEG$_{5k}$-TRC105, as-synthesized UCNP@HMSN were first functionalized with –NH_2 groups using APTES, as reported previously [25]. Briefly, UCNP@HMSN were dispersed in 20 mL of absolute ethanol, followed by addition of 1 mL of APTES. The system was sealed and kept at 86–90 °C in a water bath for 24 h. Afterwards, the mixture was centrifuged and washed several times with ethanol to remove the residual APTES. As-synthesized UCNP@HMSN-NH_2 was well dispersed in water, and the concentration of –NH_2 groups (nmol·mL^{-1}) was measured using a Kaiser test kit. Subsequently, 250 μL of UCNP@HMSN-NH_2 at ~ 1 mg·mL^{-1} in HEPES buffer

(pH 7.5, 0.1 M) was mixed with 3 mCi (or 111 MBq) of ^{89}Zr-oxalate at 75 °C for 2–3 h at pH 7–8. As-synthesized UCNP@[^{89}Zr]HMSN-NH_2 were easily collected by centrifugation at 21,000*g* for 10 min. Subsequently, a PEGylation step was introduced by reacting UCNP@[^{89}Zr]HMSN-NH_2 with SCM-PEG_{5k}-Mal (5 mg) at pH 7 for 2 h, forming UCNP@[^{89}Zr]HMSN-PEG_{5k}-Mal. UCNP@[^{89}Zr]HMSN-PEG_{5k}-TRC105 was obtained by reacting UCNP@[^{89}Zr]HMSN-PEG_{5k}-Mal with TRC105-SH in PBS at room temperature, as reported previously [23, 41].

4.8 Flow cytometry study

Cells were first harvested and suspended in cold PBS with 2% bovine serum albumin at 5 × 10^6 cells·mL^{-1} and incubated with fluorescein-conjugated UCNP@HMSN-PEG_{5k}-TRC105 (targeted group) or fluorescein-conjugated UCNP@HMSN-PEG_{5k} (non-targeted group) for 30 min at room temperature. The same fluorescein-conjugated UCNP@HMSN-PEG_{5k} were used to prepare fluorescein-conjugated UCNP@HMSN-PEG5k-TRC105 (targeted group) and fluorescein-conjugated UCNP@HMSN-PEG_{5k} (non-targeted group) in order to maintain the exact same fluorescein/nanoparticle ratio during the flow cytometry studies. The cells were washed three times with cold PBS and centrifuged for 5 min. Subsequently, the cells were washed and analyzed using a BD FACSCalibur four-color analysis cytometer, which is equipped with 488-nm and 633-nm lasers (Becton-Dickinson, San Jose, CA) and FlowJo analysis software (Tree Star, Ashland, OR). "Blocking" experiment was also performed in cells incubated with the same amount of fluorescein-conjugated UCNP@HMSN-PEG_{5k}-TRC105, where 500 μg·mL^{-1} unconjugated TRC105 was added to evaluate the specificity of fluorescein-conjugated UCNP@HMSN-PEG_{5k}-TRC105 toward CD105. The cells were also examined under a Nikon Eclipse Ti microscope to validate the results.

4.9 4T1 tumor model

All animal studies were conducted following a protocol approved by the University of Wisconsin Institutional Animal Care and Use Committee. To generate the 4T1 tumor model, 4- to 5-week-old female BALB/c mice were purchased from Envigo (Indianapolis, IN, USA), and tumors were established by subcutaneously injecting 2 × 10^6 cells, suspended in 100 μL of 1:1 mixture of RPMI 1640 and Matrigel (BD Biosciences, Franklin Lakes, NJ, USA), into the front flank of the mice. The tumor sizes were monitored every other day, and the animals were subjected to *in vivo* experiments when the tumor diameter reached 5–8 mm.

4.10 *In vivo* tumor vasculature-targeted PET imaging and biodistribution studies

PET scans at various time points post-injection were performed using a microPET/microCT Inveon rodent model scanner (Siemens Medical Solutions USA, Inc.) Image reconstruction and region-of-interest analysis of the PET data were performed similar to previously described protocols [41, 68–71]. Quantitative PET data were presented as %ID·g^{-1}. Tumor-bearing mice were each injected with 5–10 MBq of UCNP@[^{89}Zr]HMSN-PEG_{5k}-TRC105 (targeted group, ~ 32 μg of nanoparticles) or UCNP@[^{89}Zr]HMSN-PEG_{5k} (non-targeted group, ~ 32 μg of nanoparticles) via the tail. Another group of three 4T1 tumor-bearing mice were each injected with 1 mg of unlabeled TRC105 at 1 h before UCNP@[^{89}Zr]HMSN-PEG_{5k}-TRC105 administration to evaluate the CD105-targeting specificity of UCNP@[^{89}Zr]HMSN-PEG_{5k}-TRC105 *in vivo* (blocking group). After the last PET scans at 48 h p.i., biodistribution studies were carried out. The mice were euthanized, and the blood, 4T1 tumor, and major organs/tissues were collected and wet-weighed. The radioactivity in the tissue was measured using a gamma-counter (Perkin-Elmer) and presented as %ID·g^{-1} (mean ± SD).

Acknowledgements

This work is supported, in part, by the University of Wisconsin-Madison, the National Institutes of Health (P30CA014520 and NIBIB/NCI 1R01CA169365), the National Natural Science Foundation of China (No. 81630049), and the American Cancer Society (No. 125246-RSG-13-099-01-CCE).

Electronic Supplementary Material: Supplementary material (TEM images and quantitative data of ^{89}Zr-labeling, PET, and biodistribution studies) is available

in the online version of this article at https://doi.org/10.1007/s12274-2078-9.

References

[1] Ledford, H. Bankruptcy filing worries developers of nanoparticle cancer drugs. *Nature* **2016**, *533*, 304–305.

[2] Shi, J.; Kantoff, P. W.; Wooster, R.; Farokhzad, O. C. Cancer nanomedicine: Progress, challenges and opportunities. *Nat. Rev. Cancer* **2017**, *17*, 20–37.

[3] Hare, J. I.; Lammers, T.; Ashford, M. B.; Puri, S.; Storm, G.; Barry, S. T. Challenges and strategies in anti-cancer nanomedicine development: An industry perspective. *Adv. Drug Deliv. Rev.* **2017**, *108*, 25–38.

[4] Davis, M. E.; Chen, Z.; Shin, D. M. Nanoparticle therapeutics: An emerging treatment modality for cancer. *Nat. Rev. Drug Discov.* **2008**, *7*, 771–782.

[5] Chen, H. M.; Zhang, W. Z.; Zhu, G. Z.; Xie, J.; Chen, X. Y. Rethinking cancer nanotheranostics. *Nat. Rev. Mater.* **2017**, *2*, 17024.

[6] Bradbury, M. S.; Pauliah, M.; Zanzonico, P.; Wiesner, U.; Patel, S. Intraoperative mapping of sentinel lymph node metastases using a clinically translated ultrasmall silica nanoparticle. *Wiley Interdiscip. Rev. Nanomed. Nanobiotechnol.* **2016**, *8*, 535–553.

[7] Croissant, J. G.; Fatieiev, Y.; Khashab, N. M. Degradability and clearance of silicon, organosilica, silsesquioxane, silica mixed oxide, and mesoporous silica nanoparticles. *Adv. Mater.* **2017**, *29*, 1604634.

[8] Purbia, R.; Paria, S. Yolk/shell nanoparticles: Classifications, synthesis, properties, and applications. *Nanoscale* **2015**, *7*, 19789–19873.

[9] Piao, Y. Z.; Burns, A.; Kim, J.; Wiesner, U.; Hyeon, T. Designed fabrication of silica-based nanostructured particle systems for nanomedicine applications. *Adv. Funct. Mater.* **2008**, *18*, 3745–3758.

[10] Benezra, M.; Penate-Medina, O.; Zanzonico, P. B.; Schaer, D.; Ow, H.; Burns, A.; DeStanchina, E.; Longo, V.; Herz, E.; Iyer, S. et al. Multimodal silica nanoparticles are effective cancer-targeted probes in a model of human melanoma. *J. Clin. Invest.* **2011**, *121*, 2768–2780.

[11] Phillips, E.; Penate-Medina, O.; Zanzonico, P. B.; Carvajal, R. D.; Mohan, P.; Ye, Y. P.; Humm, J.; Gönen, M.; Kalaigian, H.; Schöder, H. et al. Clinical translation of an ultrasmall inorganic optical-pet imaging nanoparticle probe. *Sci. Transl. Med.* **2014**, *6*, 260ra149.

[12] Chen, F.; Ma, K.; Benezra, M.; Zhang, L.; Cheal, S. M.; Phillips, E.; Yoo, B.; Pauliah, M.; Overholtzer, M.; Zanzonico, P. et al. Cancer-targeting ultrasmall silica nanoparticles for clinical translation: Physicochemical structure and biological property correlations. *Chem. Mater.* **2017**, *29*, 8766–8779.

[13] Chen, F.; Ma, K.; Zhang, L.; Madajewski, B.; Zanzonico, P.; Sequeira, S.; Gonen, M.; Wiesner, U.; Bradbury, M. S. Target-or-clear zirconium-89 labeled silica nanoparticles for enhanced cancer-directed uptake in melanoma: A comparison of radiolabeling strategies. *Chem. Mater.* **2017**, *29*, 8269–8281.

[14] Chen, F.; Zhang, X. L.; Ma, K.; Madajewski, B.; Benezra, M.; Zhang, L.; Phillips, E.; Turker, M. Z.; Gallazzi, F.; Penate-Medina, O. et al. Melanocortin-1 receptor-targeting ultrasmall silica nanoparticles for dual-modality human melanoma imaging. *ACS Appl. Mater. Interfaces* **2018**, *10*, 4379–4393.

[15] Chen, F.; Goel, S.; Valdovinos, H. F.; Luo, H. M.; Hernandez, R.; Barnhart, T. E.; Cai, W. B. *In vivo* integrity and biological fate of chelator-free zirconium-89-labeled mesoporous silica nanoparticles. *ACS Nano* **2015**, *9*, 7950–7959.

[16] Shaffer, T. M.; Wall, M. A.; Harmsen, S.; Longo, V. A.; Drain, C. M.; Kircher, M. F.; Grimm, J. Silica nanoparticles as substrates for chelator-free labeling of oxophilic radioisotopes. *Nano Lett.* **2015**, *15*, 864–868.

[17] Shaffer, T. M.; Harmsen, S.; Khwaja, E.; Kircher, M. F.; Drain, C. M.; Grimm, J. Stable radiolabeling of sulfur-functionalized silica nanoparticles with copper-64. *Nano Lett.* **2016**, *16*, 5601–5604.

[18] Ellison, P. A.; Chen, F.; Goel, S.; Barnhart, T. E.; Nickles, R. J.; DeJesus, O. T.; Cai, W. B. Intrinsic and stable conjugation of thiolated mesoporous silica nanoparticles with radioarsenic. *ACS Appl. Mater. Interfaces* **2017**, *9*, 6772–6781.

[19] Chen, F.; Valdovinos, H. F.; Hernandez, R.; Goel, S.; Barnhart, T. E.; Cai, W. B. Intrinsic radiolabeling of titanium-45 using mesoporous silica nanoparticles. *Acta Pharmacol. Sin.* **2017**, *38*, 907–913.

[20] Lee, J. E.; Lee, N.; Kim, T.; Kim, J.; Hyeon, T. Multifunctional mesoporous silica nanocomposite nanoparticles for theranostic applications. *Acc. Chem. Res.* **2011**, *44*, 893–902.

[21] Tang, F. Q.; Li, L. L.; Chen, D. Mesoporous silica nanoparticles: Synthesis, biocompatibility and drug delivery. *Adv. Mater.* **2012**, *24*, 1504–1534.

[22] Chen, Y.; Chen, H. R.; Zeng, D. P.; Tian, Y. B.; Chen, F.; Feng, J. W.; Shi, J. L. Core/shell structured hollow mesoporous nanocapsules: A potential platform for simultaneous cell imaging and anticancer drug delivery. *ACS Nano* **2010**, *4*, 6001–6013.

[23] Chen, F.; Hong, H.; Zhang, Y.; Valdovinos, H. F.; Shi, S. X.; Kwon, G. S.; Theuer, C. P.; Barnhart, T. E.; Cai, W. B. *In vivo* tumor targeting and image-guided drug delivery with antibody-conjugated, radiolabeled mesoporous silica nanoparticles. *ACS Nano* **2013**, *7*, 9027–9039.

[24] Chen, F.; Hong, H.; Goel, S.; Graves, S. A.; Orbay, H.; Ehlerding, E. B.; Shi, S. X.; Theuer, C. P.; Nickles, R. J.; Cai, W. B. *In vivo* tumor vasculature targeting of CuS@MSN based

theranostic nanomedicine. *ACS Nano* **2015**, *9*, 3926–3934.

[25] Chen, F.; Hong, H.; Shi, S. X.; Goel, S.; Valdovinos, H. F.; Hernandez, R.; Theuer, C. P.; Barnhart, T. E.; Cai, W. B. Engineering of hollow mesoporous silica nanoparticles for remarkably enhanced tumor active targeting efficacy. *Sci. Rep.* **2014**, *4*, 5080.

[26] Shi, S. X.; Chen, F.; Cai, W. B. Biomedical applications of functionalized hollow mesoporous silica nanoparticles: Focusing on molecular imaging. *Nanomedicine* **2013**, *8*, 2027–2039.

[27] Liu, J.; Qiao, S. Z.; Budi Hartono, S.; Lu, G. Q. Monodisperse yolk-shell nanoparticles with a hierarchical porous structure for delivery vehicles and nanoreactors. *Angew. Chem., Int. Ed.* **2010**, *49*, 4981–4985.

[28] Chen, D.; Li, L. L.; Tang, F. Q.; Qi, S. Facile and scalable synthesis of tailored silica "nanorattle" structures. *Adv. Mater.* **2009**, *21*, 3804–3807.

[29] Fan, W. P.; Shen, B.; Bu, W. B.; Chen, F.; Zhao, K. L.; Zhang, S. J.; Zhou, L. P.; Peng, W. J.; Xiao, Q. F.; Xing, H. Y. et al. Rattle-structured multifunctional nanotheranostics for synergetic chemo-/radiotherapy and simultaneous magnetic/luminescent dual-mode imaging. *J. Am. Chem. Soc.* **2013**, *135*, 6494–6503.

[30] Liu, J. N.; Liu, Y.; Bu, W. B.; Bu, J. W.; Sun, Y.; Du, J. L.; Shi, J. L. Ultrasensitive nanosensors based on upconversion nanoparticles for selective hypoxia imaging *in vivo* upon near-infrared excitation. *J. Am. Chem. Soc.* **2014**, *136*, 9701–9709.

[31] Liu, Y. Y.; Liu, Y.; Bu, W. B.; Xiao, Q. F.; Sun, Y.; Zhao, K. L.; Fan, W. P.; Liu, J. N.; Shi, J. L. Radiation-/hypoxia-induced solid tumor metastasis and regrowth inhibited by hypoxia-specific upconversion nanoradiosensitizer. *Biomaterials* **2015**, *49*, 1–8.

[32] Chen, Y.; Chen, H. R.; Guo, L. M.; He, Q. J.; Chen, F.; Zhou, J.; Feng, J. W.; Shi, J. L. Hollow/rattle-type mesoporous nanostructures by a structural difference-based selective etching strategy. *ACS Nano* **2010**, *4*, 529–539.

[33] Zhang, Q.; Zhang, T. R.; Ge, J. P.; Yin, Y. D. Permeable silica shell through surface-protected etching. *Nano Lett.* **2008**, *8*, 2867–2871.

[34] Lin, L. S.; Song, J. B.; Yang, H. H.; Chen, X. Y. Yolk-shell nanostructures: Design, synthesis, and biomedical applications. *Adv. Mater.* **2018**, *30*, 1704639.

[35] Liu, J.; Qiao, S. Z.; Chen, J. S.; Lou, X. W.; Xing, X. R.; Lu, G. Q. Yolk/shell nanoparticles: New platforms for nanoreactors, drug delivery and lithium-ion batteries. *Chem. Commun.* **2011**, *47*, 12578–12591.

[36] Priebe, M.; Fromm, K. M. Nanorattles or yolk-shell nanoparticles--what are they, how are they made, and what are they good for? *Chem.—Eur. J.* **2015**, *21*, 3854–3874.

[37] Fang, J.; Nakamura, H.; Maeda, H. The EPR effect: Unique features of tumor blood vessels for drug delivery, factors involved, and limitations and augmentation of the effect. *Adv. Drug Deliv. Rev.* **2011**, *63*, 136–151.

[38] Chen, F.; Cai, W. B. Tumor vasculature targeting: A generally applicable approach for functionalized nanomaterials. *Small* **2014**, *10*, 1887–1893.

[39] Seon, B. K.; Haba, A.; Matsuno, F.; Takahashi, N.; Tsujie, M.; She, X. W.; Harada, N.; Uneda, S.; Tsujie, T.; Toi, H. et al. Endoglin-targeted cancer therapy. *Curr. Drug Deliv.* **2011**, *8*, 135–143.

[40] Rosen, L. S.; Hurwitz, H. I.; Wong, M. K.; Goldman, J.; Mendelson, D. S.; Figg, W. D.; Spencer, S.; Adams, B. J.; Alvarez, D.; Seon, B. K. et al. A phase I first-in-human study of TRC105 (anti-endoglin antibody) in patients with advanced cancer. *Clin. Cancer Res.* **2012**, *18*, 4820–4829.

[41] Hong, H.; Yang, K.; Zhang, Y.; Engle, J. W.; Feng, L. Z.; Yang, Y.; Nayak, T. R.; Goel, S.; Bean, J.; Theuer, C. P. et al. *In vivo* targeting and imaging of tumor vasculature with radiolabeled, antibody-conjugated nanographene. *ACS Nano* **2012**, *6*, 2361–2370.

[42] Chen, F.; Nayak, T. R.; Goel, S.; Valdovinos, H. F.; Hong, H.; Theuer, C. P.; Barnhart, T. E.; Cai, W. B. *In vivo* tumor vasculature targeted PET/NIRF imaging with TRC105(fab)-conjugated, dual-labeled mesoporous silica nanoparticles. *Mol. Pharmaceutics* **2014**, *11*, 4007–4014.

[43] Goel, S.; Chen, F.; Luan, S. J.; Valdovinos, H. F.; Shi, S. X.; Graves, S. A.; Ai, F. R.; Barnhart, T. E.; Theuer, C. P.; Cai, W. B. Engineering intrinsically zirconium-89 radiolabeled self-destructing mesoporous silica nanostructures for *in vivo* biodistribution and tumor targeting studies. *Adv. Sci.* **2016**, *3*, 1600122.

[44] Zhou, J.; Liu, Z.; Li, F. Y. Upconversion nanophosphors for small-animal imaging. *Chem. Soc. Rev.* **2012**, *41*, 1323–1349.

[45] Haase, M.; Schäfer, H. Upconverting nanoparticles. *Angew. Chem., Int. Ed.* **2011**, *50*, 5808–5829.

[46] Ju, Q.; Tu, D. T.; Liu, Y. S.; Li, R. F.; Zhu, H. M.; Chen, J. C.; Chen, Z.; Huang, M. D.; Chen, X. Y. Amine-functionalized lanthanide-doped $KGdF_4$ nanocrystals as potential optical/magnetic multimodal bioprobes. *J. Am. Chem. Soc.* **2012**, *134*, 1323–1330.

[47] Wu, S. W.; Han, G.; Milliron, D. J.; Aloni, S.; Altoe, V.; Talapin, D. V.; Cohen, B. E.; Schuck, P. J. Non-blinking and photostable upconverted luminescence from single lanthanide-doped nanocrystals. *Proc. Natl. Acad. Sci. USA* **2009**, *106*, 10917–10921.

[48] Cheng, L.; Wang, C.; Liu, Z. Upconversion nanoparticles and their composite nanostructures for biomedical imaging and cancer therapy. *Nanoscale* **2013**, *5*, 23–37.

[49] Park, Y. I.; Kim, J. H.; Lee, K. T.; Jeon, K. S.; Bin Na, H.; Yu, J. H.; Kim, H. M.; Lee, N.; Choi, S. H.; Baik, S. I. et al. Nonblinking and nonbleaching upconverting nanoparticles as

an optical imaging nanoprobe and T1 magnetic resonance imaging contrast agent. *Adv. Mater.* **2009**, *21*, 4467–4471.

[50] Chatterjee, D. K.; Rufaihah, A. J.; Zhang, Y. Upconversion fluorescence imaging of cells and small animals using lanthanide doped nanocrystals. *Biomaterials* **2008**, *29*, 937–943.

[51] Nam, S. H.; Bae, Y. M.; Park, Y. I.; Kim, J. H.; Kim, H. M.; Choi, J. S.; Lee, K. T.; Hyeon, T.; Suh, Y. D. Long-term real-time tracking of lanthanide ion doped upconverting nanoparticles in living cells. *Angew. Chem., Int. Ed.* **2011**, *50*, 6093–6097.

[52] Xiong, L. Q.; Chen, Z. G.; Tian, Q. W.; Cao, T. Y.; Xu, C. J.; Li, F. Y. High contrast upconversion luminescence targeted imaging *in vivo* using peptide-labeled nanophosphors. *Anal. Chem.* **2009**, *81*, 8687–8694.

[53] Chen, F.; Bu, W. B.; Zhang, S. J.; Liu, J. N.; Fan, W. P.; Zhou, L. P.; Peng, W. J.; Shi, J. L. Gd^{3+}-ion-doped upconversion nanoprobes: Relaxivity mechanism probing and sensitivity optimization. *Adv. Funct. Mater.* **2013**, *23*, 298–307.

[54] Chen, F.; Bu, W. B.; Zhang, S. J.; Liu, X. H.; Liu, J. N.; Xing, H. Y.; Xiao, Q. F.; Zhou, L. P.; Peng, W. J.; Wang, L. Z. et al. Positive and negative lattice shielding effects co-existing in Gd (III) ion doped bifunctional upconversion nanoprobes. *Adv. Funct. Mater.* **2011**, *21*, 4285–4294.

[55] Chen, F.; Bu, W. B.; Chen, Y.; Fan, Y. C.; He, Q. J.; Zhu, M.; Liu, X. H.; Zhou, L. P.; Zhang, S. J.; Peng, W. J. et al. A sub-50-nm monosized superparamagnetic Fe_3O_4@SiO_2 T_2-weighted MRI contrast agent: Highly reproducible synthesis of uniform single-loaded core-shell nanostructures. *Chem.—Asian J.* **2009**, *4*, 1809–1816.

[56] Taylor, K. M. L.; Kim, J. S.; Rieter, W. J.; An, H. Y.; Lin, W. L.; Lin, W. B. Mesoporous silica nanospheres as highly efficient MRI contrast agents. *J. Am. Chem. Soc.* **2008**, *130*, 2154–2155.

[57] Fang, X. L.; Chen, C.; Liu, Z. H.; Liu, P. X.; Zheng, N. F. A cationic surfactant assisted selective etching strategy to hollow mesoporous silica spheres. *Nanoscale* **2011**, *3*, 1632–1639.

[58] Chen, F.; Ellison, P. A.; Lewis, C. M.; Hong, H.; Zhang, Y.; Shi, S. X.; Hernandez, R.; Meyerand, M. E.; Barnhart, T. E.; Cai, W. B. Chelator-free synthesis of a dual-modality PET/MRI agent. *Angew. Chem., Int. Ed.* **2013**, *52*, 13319–13323.

[59] Zhuravlev, L. T. The surface chemistry of amorphous silica. Zhuravlev model. *Colloids Surf. A* **2000**, *173*, 1–38.

[60] Fonsatti, E.; Nicolay, H. J.; Altomonte, M.; Covre, A.; Maio, M. Targeting cancer vasculature via endoglin/CD105: A novel antibody-based diagnostic and therapeutic strategy in solid tumours. *Cardiovasc. Res.* **2010**, *86*, 12–19.

[61] Tian, B.; Wang, Q. H.; Su, Q. Q.; Feng, W.; Li, F. Y. *In vivo* biodistribution and toxicity assessment of triplet-triplet annihilation-based upconversion nanocapsules. *Biomaterials* **2017**, *112*, 10–19.

[62] Sun, Y.; Feng, W.; Yang, P. Y.; Huang, C. H.; Li, F. Y. The biosafety of lanthanide upconversion nanomaterials. *Chem. Soc. Rev.* **2015**, *44*, 1509–1525.

[63] Feng, Q. Y.; Liu, Y. P.; Huang, J.; Chen, K.; Huang, J. X.; Xiao, K. Uptake, distribution, clearance, and toxicity of iron oxide nanoparticles with different sizes and coatings. *Sci. Rep.* **2018**, *8*, 2082.

[64] Singh, N.; Jenkins, G. J. S.; Asadi, R.; Doak, S. H. Potential toxicity of superparamagnetic iron oxide nanoparticles (SPION). *Nano Rev.* **2010**, *1*, 5358.

[65] Tsoi, K. M.; Dai, Q.; Alman, B. A.; Chan, W. C. W. Are quantum dots toxic? Exploring the discrepancy between cell culture and animal studies. *Acc. Chem. Res.* **2013**, *46*, 662–671.

[66] Ye, L.; Yong, K. T.; Liu, L. W.; Roy, I.; Hu, R.; Zhu, J.; Cai, H. X.; Law, W. C.; Liu, J. W.; Wang, K. et al. A pilot study in non-human primates shows no adverse response to intravenous injection of quantum dots. *Nat. Nanotechnol.* **2012**, *7*, 453–458.

[67] Zhang, Y.; Hong, H.; Severin, G. W.; Engle, J. W.; Yang, Y.; Goel, S.; Nathanson, A. J.; Liu, G.; Nickles, R. J.; Leigh, B. R. et al. ImmunoPET and near-infrared fluorescence imaging of CD105 expression using a monoclonal antibody dual-labeled with ^{89}Zr and IRDye 800CW. *Am. J. Transl. Res.* **2012**, *4*, 333–346.

[68] Zhang, Y.; Hong, H.; Orbay, H.; Valdovinos, H. F.; Nayak, T. R.; Theuer, C. P.; Barnhart, T. E.; Cai, W. B. PET imaging of CD105/endoglin expression with a $^{61/64}$Cu-labeled Fab antibody fragment. *Eur. J. Nucl. Med. Mol. Imaging* **2013**, *40*, 759–767.

[69] Zhang, Y.; Hong, H.; Engle, J. W.; Yang, Y.; Barnhart, T. E.; Cai, W. Positron emission tomography and near-infrared fluorescence imaging of vascular endothelial growth factor with dual-labeled bevacizumab. *Am. J. Nucl. Med. Mol. Imaging* **2012**, *2*, 1–13.

[70] Shi, S. X.; Yang, K.; Hong, H.; Valdovinos, H. F.; Nayak, T. R.; Zhang, Y.; Theuer, C. P.; Barnhart, T. E.; Liu, Z.; Cai, W. B. Tumor vasculature targeting and imaging in living mice with reduced graphene oxide. *Biomaterials* **2013**, *34*, 3002–3009.

[71] Hong, H.; Zhang, Y.; Severin, G. W.; Yang, Y.; Engle, J. W.; Niu, G.; Nickles, R. J.; Chen, X. Y.; Leigh, B. R.; Barnhart, T. E. et al. Multimodality imaging of breast cancer experimental lung metastasis with bioluminescence and a monoclonal antibody dual-labeled with ^{89}Zr and IRDye 800CW. *Mol. Pharmaceutics* **2012**, *9*, 2339–2349.